processes

MDPI

Article

Multimodal Data Fusion System for Accurate Identification of Impact Points on Rocks in Mining Comminution Tasks

John Kern, Daniel Fernando Quintero Bernal * and Claudio Urrea

Electrical Engineering Department, Faculty of Engineering, University of Santiago of Chile (USACH), Av. Víctor Jara 3519, Estación Central, Santiago 9170124, Chile; john.kern@usach.cl (J.K.); claudio.urrea@usach.cl (C.U.)

* Correspondence: daniel.quintero@usach.cl

Abstract: This study presents a multimodal data fusion system to identify and impact rocks in mining comminution tasks, specifically during the crushing stage. The system integrates information from various sensory modalities to enhance data accuracy, even under challenging environmental conditions such as dust and lighting variations. For the strategy selected in this study, 15 rock characteristics are extracted at neighborhood radii of 5 mm, 10 mm, 15 mm, 20 mm, and 25 mm to determine the suitable impact points. Through processes like the Ball−Pivoting Algorithm (BPA) and Poisson Surface Reconstruction techniques, the study achieves a detailed reconstruction of filtered points based on the selected characteristics. Unlike related studies focused on controlled conditions or limited analysis of specific rock shapes, this study examines all rock faces, ensuring the more accurate identification of impact points under adverse conditions. Results show that rock faces with the largest support areas are most suitable for receiving impacts, enhancing the efficiency and stability of the crushing process. This approach addresses the limitations of manual operations and provides a pathway for reducing operational costs and energy consumption. Furthermore, it establishes a robust foundation for future research to develop fully autonomous systems capable of maintaining reliable performance in extreme mining environments.

Keywords: crushing; data fusion; mining comminution; multimodal; rocks

check for updates

Academic Editors: Junyao Xie, Wanke Yu, Shumei Zhang and Yiyang Chen

Received: 22 November 2024
Revised: 28 December 2024
Accepted: 30 December 2024
Published: 2 January 2025

Citation: Kern, J.; Quintero Bernal, D.F.; Urrea, C. Multimodal Data Fusion System for Accurate Identification of Impact Points on Rocks in Mining Comminution Tasks. *Processes* **2025**, *13*, 87. https://doi.org/10.3390/pr13010087

Copyright: © 2025 by the authors. Licensee MDPI, Basel, Switzerland. This article is an open access article distributed under the terms and conditions of the Creative Commons Attribution (CC BY) license (https://creativecommons.org/licenses/by/4.0/).

1. Introduction

Multimodal data fusion is a critical field in the scientific domain, integrating information from multiple sensory sources to enhance data analysis. This technique is particularly relevant in the mining industry, where combining modalities with varying dimensionalities and temporalities is essential for addressing specific tasks in complex environments. Data fusion enables the utilization of heterogeneous information, and offers significant advantages in terms of efficiency and robustness by reducing noise and improving the quality of the collected data.

The IDeA I + D ID21I10087 project focuses on improving the crushing stage within mining comminution tasks by incorporating a multisensory system designed as part of a retrofittable kit for existing rock−breaking hammers. These hammers are intended to adjust the size of rocks before they enter the milling stage, ensuring they reach the dimensions necessary for efficient mineral liberation.

Effective crushing not only conditions the milling material but also contributes to greater process efficiency by reducing the workload on the mill, which can translate into significant energy savings. According to the consulted literature, efficient crushing can

achieve rock size reductions comparable to those obtained during milling while using approximately half the energy and associated costs [1].

A fundamental objective of the project is the identification, tracking, and precise selection of impact points on rocks to mitigate operational costs and enhance productivity. This includes addressing the downtime caused by rock accumulations and blockages, which occur when rocks are not effectively fractured during crushing due to visual occlusion by operators, dust, and other adverse environmental conditions typical of mining sites. Additionally, the system is designed to limit the energy consumption associated with repetitive impacts, often performed during manual operations, by ensuring the accurate identification of the most effective impact points.

Other studies have explored similar approaches. Lampinen et al. (2021) proposed an autonomous rock−breaking system that employs a Visual Perception System (VPS) and an industrial manipulator to determine the breaking order. However, the stereo camera demonstrated limitations under adverse conditions, such as snow and dust, highlighting the need for more robust systems [2]. Correa et al. (2022) developed a haptic teleoperation system for impact hammers in underground mining, addressing issues such as latency and limited visibility. However, the researchers conducted their tests in controlled environments without evaluating rock shapes, which limits their applicability in real−world scenarios [3]. Cárdenas et al. (2022) introduced an automated system that segments rocks using point clouds and images to enhance impact operations in mining. Nonetheless, by restricting their experiments to controlled environments, the practical applicability of their approach is constrained [4].

Samtani et al. (2023) proposed an autonomous rock−breaking system using deep reinforcement learning (DRL) with the Dueling Double Deep Q−Learning Neural Network (DDDQN). While effectively reducing failed impacts, the system faces challenges in transferring learned policies from the simulated to the real environment and achieving precision on irregular surfaces [5]. Similarly, Li et al. (2024) introduced a sensor fusion system combining RGB cameras and a Light Detection And Ranging sensor (LiDAR) to detect impact surfaces, employing the Random Sample Consensus (RANSAC) algorithm to enhance fracture point identification accuracy. However, this approach is limited to analyzing only the top face of the rock, unlike the present study, which examines all faces to identify the most stable one. Although sensor fusion improves lighting management, the system requires validation under more adverse conditions, such as rain and snow, to ensure its effectiveness [6,7].

This study addresses the limitations identified in previous research by developing a robust and adaptable system to the demands of challenging mining environments. The study emphasizes selecting appropriate sensory modalities to operate efficiently under adverse conditions, such as dust, lighting variations, and fog. The proposed system enables the precise identification of impact points by analyzing the specific shapes of rocks, significantly improving the mining industry's crushing processes.

2. Materials and Methods

This research is associated with project I + D ID21I10087, which aims to develop a system adaptable to industrial "rock−pick hammer" equipment for performing tasks in mining comminution. This system aims to improve the crushing stage, which is essential for adjusting the size of rocks before they enter the grinding process. By refining this process, the system ensures that the rocks reach the necessary size for efficient mineral liberation during grinding [1]. The system aims to minimize the downtime caused by accumulations and blockages of rocks that have not been effectively fractured during crushing through

the identification, tracking, and selective impact on rocks. In addition, it seeks to reduce the energy consumption associated with repetitive impacts carried out in manual operations.

In line with the project, this research's advances are aligned with three key objectives: the development of a multisensory system, the implementation of algorithms for rock dimensionalization, and the creation of computational machine learning models.

The following subsections detail the critical components of the study, including the scenarios considered, the selection of sensory modalities, the proposed data fusion architecture, and the methodology for identifying impact points.

2.1. Considered Scenarios and Modality Selection

In the crushing process, a critical stage in comminution, an operator manually positions a breaker hammer over the rocks to be fragmented before their processing in grinding. The precise placement of the hammer and the correct angle of incidence are critical. They are significantly affected by factors such as the operator's location, the presence of airborne particles, and ambient lighting variations.

Given the adverse conditions characterizing the specific application investigated, two types of scenarios are defined (see Figure 1), each with three different rock configurations (see Figure 2). This approach allows for the evaluation of the effectiveness of the developed technology under various operating conditions.

The defined scenarios are as follows:

- Simple scenario (Figure 1a): This excludes contamination, disturbances and noise. It represents the ideal conditions without external elements interfering with the rock visualization.
- Complex scenario (Figure 1b): This scenario introduces various sources of contamination and disturbance that impact observation. These include variations in lighting conditions, ranging from high to low levels, and airborne particles such as dust and mist, which can lead to visual occlusion.

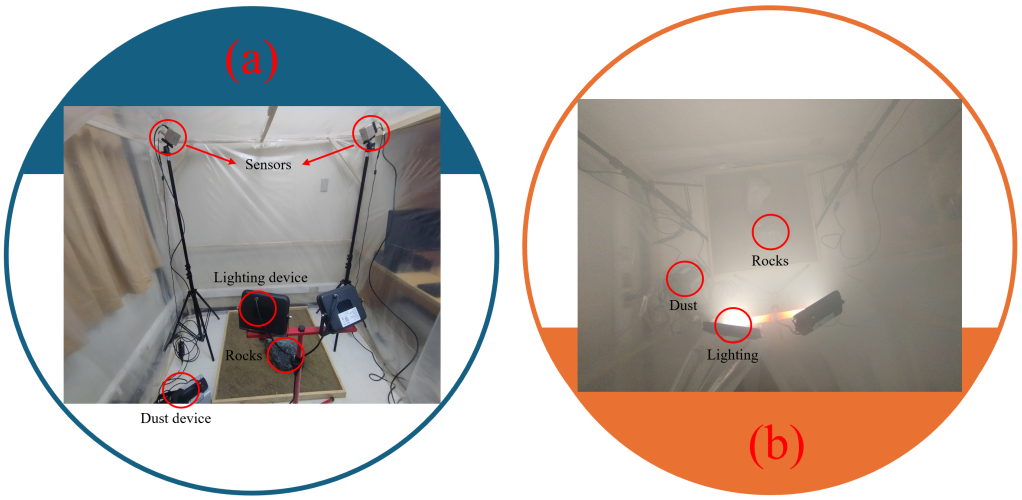

Figure 1. Considered test scenarios. (**a**) Simple scenario. (**b**) Complex scenario.

The identified rock arrangement configurations are as follows:

- Stacked rocks (Figure 2a): multiple rocks arranged in an overlapping configuration, which may complicate individual identification and analysis.
- Close rocks (Figure 2b): two or more rocks located closely together but without overlapping.
- Single rock (Figure 2c): a single rock with no proximity to others, allowing precise observation and analysis.

To specify the selected modalities, it is essential to clarify some key concepts:

- First, data fusion combines information from various sources and times to facilitate decision−making, whether manual or automated [8]. These approaches often involve merging datasets with different spatial resolutions, aiming to create a unified dataset with the finest resolution [9]. In multisensory systems, integrating data from multiple sensors is crucial for reducing detection uncertainty, which individual sensors cannot achieve. This strategy is vital for developing robust models capable of perceiving the environment under diverse ambient conditions, essential for applications like autonomous vehicles and other automated systems [10,11].
- Second, when a data fusion system considers explicitly different types of sensors, it is known as multimodal data fusion. A modality is acquiring information from a given system through a specific mode or channel. Each modality is characterized by its temporality and dimensionality. Dimensionality is classified as 1D (one−dimensional data), 2D (two−dimensional data, e.g., an image), or 3D (three−dimensional data, such as a point cloud). In terms of temporality, data can be classified as static (data without temporal designation) or time series (e.g., samples taken at specified time intervals, such as in a video) [11,12].

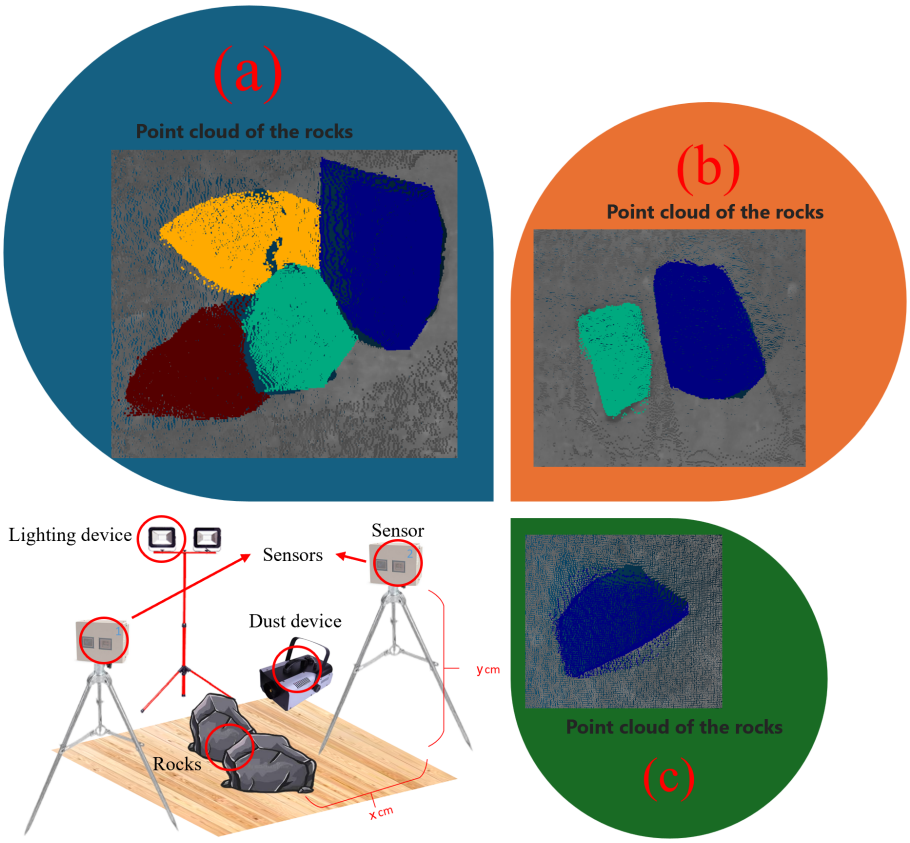

Figure 2. Rock arrangements in test scenarios. (**a**) Stacked rocks. (**b**) Close rocks. (**c**) Single rock.

Since developing a multisensory system is one of the critical objectives of the project I + D ID21I10087, an exhaustive study takes place in this area. Considering the project's resource availability, laboratory test results in the identified scenarios [13], and the recommendations of Yeong et al. [10] and Schreier [14], the following modalities are selected (Table 1):

Table 1. Selected modalities.

Reference	Modality	Dimensionality	Characteristics	Contributions
Blaze 101 [15]	ToF Camera (featuring VCSEL, Vertical Cavity Surface−Emitting Lasers, emitting invisible near−infrared laser light at 940 nm).	3D (point clouds in Coord3D_ABC32f format). 2D (depth maps in Coord3D_C16, Mono16, and Coord3D_ABC32f formats; intensity images in Mono16; and confidence maps in Mono16 and Confidence16).	The camera has a resolution of 640 × 480 pixels, providing a horizontal and vertical field of view of 67° and 51°, respectively. It can operate in two ranges: a short range from 0.3 to 1.5 m, and a long range from 0.3 to 10 m. Typical accuracy in distance measurements is ±5 mm (0.5–5.5 m).	The system demonstrates robustness in varying lighting conditions. Within its operational range, it can provide a point density suitable for detailed rock analysis.
RMS1000 [16]	Radar (FMCW, Frequency−Modulated Continuous Wave radar, operating in the 61 GHz to 61.5 GHz frequency band).	1D (distance to detected object).	The radar has a horizontal opening angle of ±60° and a vertical opening angle of ±4°. Its range is 50 m with an RCS (Radar Cross−Section) of 1 m^2 and 100 m with an RCS of 10 m^2. Distance accuracy is 0.04 m for an RCS of 1 m^2 up to 20 m and 0.1 m for an RCS of 1 m^2 up to 50 m. Distance resolution is 0.4 m.	Reliable detection in adverse environmental and visibility conditions, such as dense fog or dust. This technology ensures excellent outdoor performance, even under various lighting intensities.
CERES V 640 [17]	Thermal camera	2D	Provides a resolution of 640 × 480 pixels with a pixel size of 12 µm. The camera can capture thermal images at a maximum frame rate of 60 Hz. Its spectral range is from 8 to 14 µm due to its microbolometer detector. Additionally, it is designed to operate across a wide range of ambient temperatures, from −40 °C to +70 °C.	Allows for precise temperature calibrations for thermographic applications. It shows robustness in various industrial applications, maintaining reliable performance even in adverse environmental conditions.

Table 1. *Cont.*

Reference	Modality	Dimensionality	Characteristics	Contributions
SDS011 [18]	Laser diode	1D	Uses the laser scattering principle to measure particle concentration in the air, within a range of 0.3 µm to 10 µm with a resolution of 0.3 µg/m^3.	Provides precise air quality measurements with a rapid response to changes in environmental conditions.
BH1750FVI [19]	Ambient light sensor	1D	Can measure light intensities up to 65,535 lux.	Allows automatic exposure adjustment in vision systems.

2.2. System Schematics

This section describes, through two schematics, the physical connection of the sensors using a network topology and the conceptual model that illustrates the various procedures considered for the data fusion system.

2.2.1. Network Topology

Following the work conducted in [13], this section briefly describes the network topology. The setup establishes communication using the IPv4 protocol (RFC 791) on the 192.168.0.0/24 network segment, connecting six sensors and a computer through a layer two switch, model Cisco SF−100−16. The switch connection uses a star topology. Considering the number of devices, the configuration opts for static addressing instead of DHCP (see Figure 3).

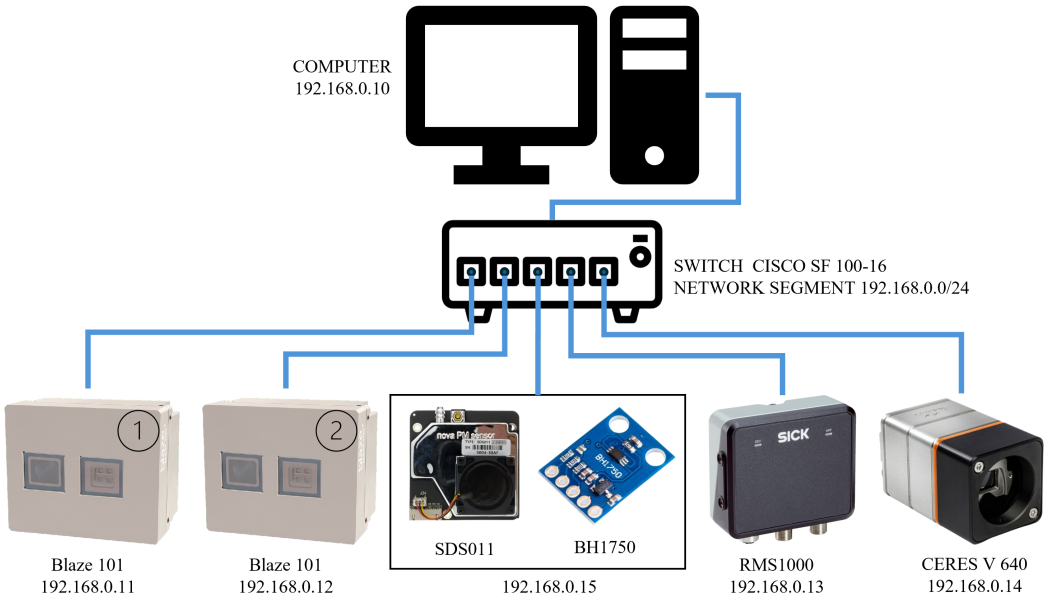

Figure 3. Network topology.

Figure 4 shows the actual system setup. This setup enables the acquisition of static data from various sensors with specific dimensionalities (see Table 1), significantly contributing to one of the critical objectives of the project I + D ID21I10087: creating computational models based on machine learning. This process facilitates the generation of databases that support parallel developments within the project. The database is primarily composed of

627 point clouds obtained from eight rocks from the "La Patagua" mine, corresponding to the two identified scenarios (simple and complex). Of these clouds, 315 correspond to stacked rock configurations, while 312 represent close or individual rock configurations. It is important to note that 100 of these samples were collected directly in a mining environment, with 50 captured under high−lighting conditions and 50 under low lighting with airborne particles (dust), typical adverse conditions in mining environments [20].

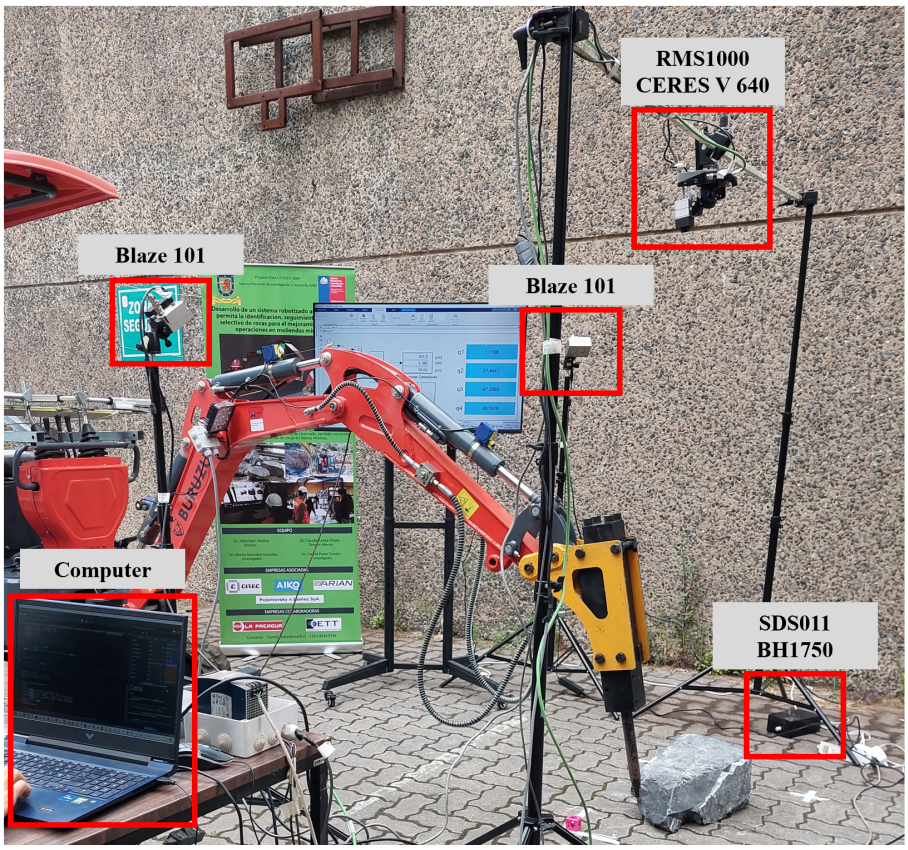

Figure 4. Real system setup.

2.2.2. Data Fusion Architecture

The following presents two interrelated architectures. The first is the global autonomy system developed within the project I + D ID21I10087, which establishes the complete framework for autonomous operation. The second architecture, integrated within the first, focuses specifically on Strategy 1, which forms the foundation of the present research.

Figure 5 illustrates the workflow of the autonomy system (first architecture). The "Data Acquisition" stage collects information from sensors of various modalities across three dimensions: 1D (RMS1000, SDS011, and BH1750), 2D (2 BLAZE 101 and CERES V 640), and 3D (2 BLAZE 101). The "Planning and Decision" stage processes the acquired data, where two key decision−making strategies are implemented based on identifying the operational scenario (simple or complex) and applied to different rock configurations (single rock, close rocks, and stacked rocks). This phase generates the coordinates (x, y, z), which are essential for precisely determining the location of impact points. Subsequently, in the "Motion and Control" stage, trajectory tracking is performed using advanced control algorithms that utilize these coordinates by the selected strategy [21,22].

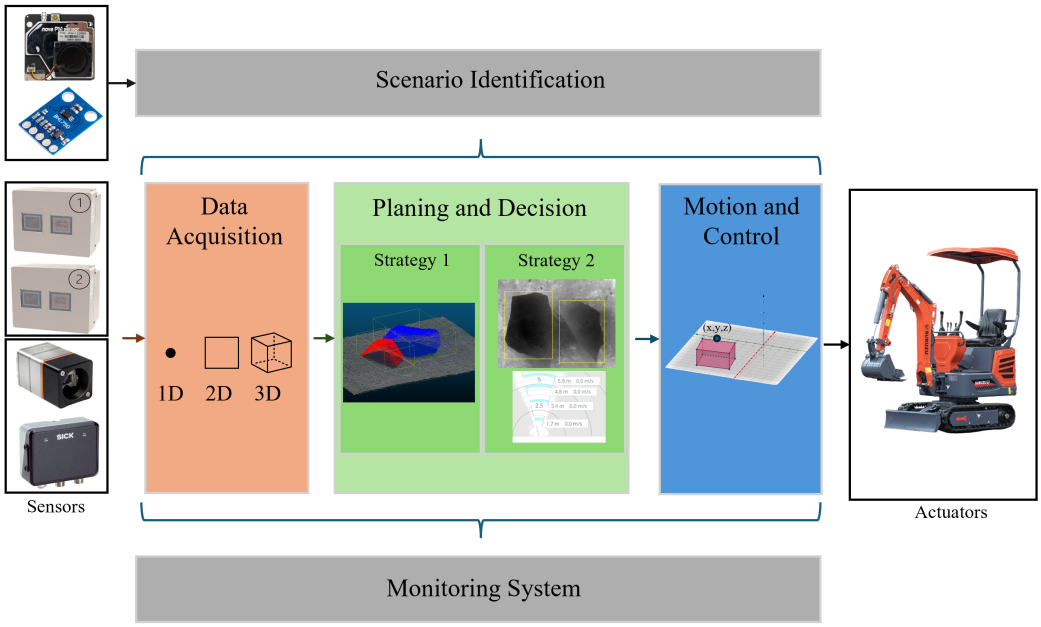

Figure 5. Autonomy system architecture.

This research focuses on the "Data Acquisition" and "Planning and Decision−Strategy 1" modules. Within the project I + D ID21I10087, other complementary studies were also conducted, such as those by Rodríguez−Guillén et al. [23], and Kern et al. [20], which focused on the "Planning and Decision−Strategy 2" stage. Additionally, the studies by Potter et al. [24], Marrero et al. [25], and Kern et al. [26] concentrated on the "Motion and Control" phase, contributing critical developments in this area.

Regarding the second architecture, due to the inherent complexity of a data fusion system, it is necessary to unify terms to specify each component's characteristics and functionalities. Therefore, this approach implements architectures that allow hierarchical management of data manipulation from various sources. Multiple models exist in the scientific literature, such as (a) JDL, (b) Dasarathy, and (c) Luo and Kay [8,27,28]. Based on [10,29], Figure 6 presents a data fusion model as part of Strategy 1.

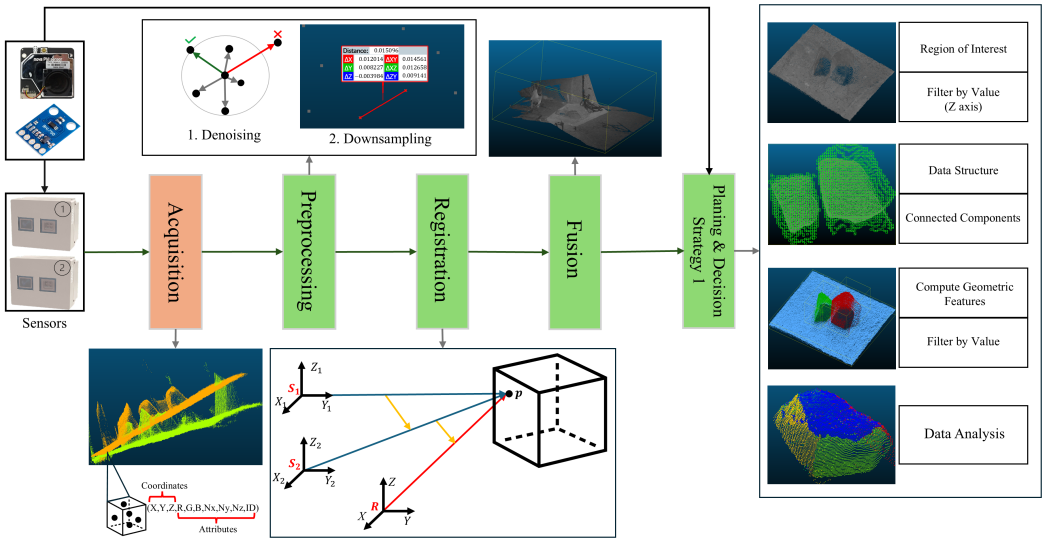

Figure 6. Data fusion system architecture.

Figure 6 clearly illustrates the stages involved in the data fusion architecture. The description below details each stage, its functionality, and specific characteristics. The

stages apply techniques that build upon the work in [13]. The team captured data using Python 3.9.15 and the Harvesters 1.4.2 library. MatLab R2023b [30], and CloudCompare 2.13.alpha [31] software processed information across the stages.

Acquisition: Data acquisition refers to obtaining information with an established temporality from various sources (sensors) that deliver specific dimensionalities due to their inherent characteristics. Section 2.2.1 provides details regarding information acquisition. The information of interest for the strategy addressed comes from the BLAZE 101 sensors, providing static 3D (point cloud) data. Notably, the justification for using two BLAZE 101 sensors is to obtain complete information from the region of interest within the point clouds, a process known as complementary data fusion [28].

A point cloud can be defined as a set of points $\{P_i, \ i = 1, \ \ldots, \ n\}$ in a three−dimensional Cartesian space, where each point P_i has coordinates x_i, y_i and z_i belonging to $\mathbb{R}^3$. Additionally, each point may have various attributes $\{a_{i,j}\}$, where $j = 1, \ \ldots, \ m_i$. These attributes can include, for example, the color of a spectral band, a component of the local surface normal vector, or a classification or segmentation identifier, thereby representing each point as $(x_i, y_i, z_i, a_{i,1}, \ldots, a_{i,m})$ [10,32,33].

Preprocessing: Preprocessing aims to reduce the points in the point clouds based on various criteria to improve algorithm efficiency. This stage involves two subprocesses: denoising and downsampling.

According to Leal Narváez in [33], a denoising problem can be modeled as $(^{p'}_{i} = p_i + \epsilon(p_i), \quad \text{for} \quad i = 1, 2, \ldots, n)$. Here, the goal is to recover the complete set of samples (p_i) from the noisy observations $(^{p'}_{i})$. The assumption is that the noise distribution $(\epsilon(p_i))$ has a zero mean and a variance of (σ^2), typically following a normal distribution. The denoising approach relies on calculating the average distance to the (k) nearest neighbors. Points considered outliers are those located beyond a predetermined threshold as shown in Equation (1):

$$\text{Threshold} = (n \cdot \text{Standard_Deviation}) + \text{Average_Distance} \tag{1}$$

The downsampling process involves selecting a subset of points from a point cloud to reduce the data quantity while preserving the relevant information and, in some cases, ensuring an adequate point density. According to Chen et al. in [34], the following describes this process: let $\mathcal{S} = \{p_i \in \mathbb{R}^3\}_{i=1}^{N}$ be a point cloud with N points. It is given that $\mathcal{S}M = h(\mathcal{S})$, where h is a reduction operator that selects M points from $\mathcal{S}$, with $M < N$. Therefore, $\mathcal{S}_{\mathcal{M}} = \{p_{\mathcal{M}_i} \in \mathbb{R}^3\}_{i=1}^{M}$ is a reduced point cloud, where the reduced set $\mathcal{M} = (\mathcal{M}_1, \ldots, \mathcal{M}_M)$ indicates the sequence of selected indices, $\mathcal{M}_i \in 1, \ldots, N$, con $|\mathcal{M}| = M$. The downsampling used a minimum distance−based approach between points. The OCTREE data structure organizes the point cloud spatially, enabling efficient analysis and filtering based on the established distance. OCTREE divides the 3D space of the point cloud into eight equal−sized cubes, and depending on the desired depth level, it can successively subdivide each non−empty cube into eight smaller cubes [35].

Registration: Data registration refers to aligning captures from different sensors, each with its reference frame, into a standard frame before fusion. This process maintains invariability over a specific period. Equation (2) shows the transformation matrix that enables the registration:

$$\begin{pmatrix} \text{R11} & \text{R12} & \text{R13} & \text{Tx} \\ \text{R21} & \text{R22} & \text{R23} & \text{Ty} \\ \text{R31} & \text{R32} & \text{R33} & \text{Tz} \\ 0 & 0 & 0 & 1 \end{pmatrix} \tag{2}$$

where (R) is the rotation matrix, and (T) is a translation vector. If (P) is any point belonging to a point cloud, a transformed point ($P^{'}$) can be expressed as ($P^{'}$) = $R \cdot P + T$) [8,10]. The following section outlines the approach (see Figure 7).

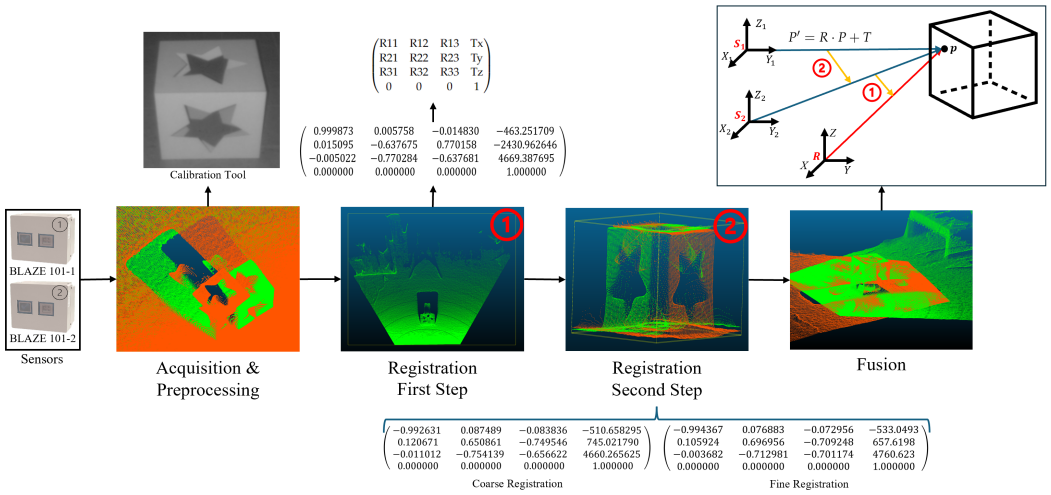

Figure 7. Point cloud registration.

First, experimentally, one of the two BLAZE 101 sensors (Basler AG, Ahrensburg, Germany) is aligned to a predetermined reference frame. Second, a two−stage registration strategy, known as "coarse−to−fine registration", is used to align the captures from the second BLAZE−101 relative to the first, which has already undergone initial registration. Additionally, an object is used as a calibration tool.

The Coarse Registration method primarily involves alignment based on surface, line, or point features. This stage applies the alignment of equivalent points on the calibration tool.

The Fine Registration method aims to achieve maximum overlap between the two point clouds. The ICP (Iterative Closest Point) technique is employed to minimize the distance between two subsets of points (a reference set (P) and a set to be aligned (Q). The alignment process uses the capture from the BLAZE−101 sensor, which has previously undergone Coarse Registration. In general, the ICP algorithm iterates as follows: (1) a correspondence subset $\mathcal{K} = \{(p, q)\}$ (representing the same area of interest in the captures from the calibration tool's sensors) is identified from P y Q transformed with the current transformation matrix T, and (2) an objective function $E(T)$ (see Equation (3)) defined over the subset $\mathcal{K}$ is minimized to update T [10,36,37]:

$$E(T) = \sum_{(p,q)\in\mathcal{K}} \|p - Tq\|^2 \tag{3}$$

Fusion: Data fusion can be implemented at three levels: (1) raw data fusion/low−level Fusion, (2) feature−level fusion/mid−level fusion, and (3) decision fusion/high−level fusion. This study applies fusion at the low−level fusion stage, combining raw data from different sensors. Some considerations include the following: (1) low−level fusion is feasible since the data have a similar structure in terms of dimensionality and spatial resolution; (2) this approach allows for obtaining refined features, along with more accurate information and less noisy data; (3) this approach is valuable for specific real−time applications, as direct data processing reduces wait times in subsequent processes, and (4) the fusion technique used consists of the direct merging of points from both captures (Figure 7) [8,10,12,14].

Planning and Decision−Strategy 1: The module composed of the SDS011 (Nova Fitness Co. Ltd., Jinan, Shandong Province, China) and BH1750 (ROHM Co. Ltd., Kyoto, Japan) sensors enables the scenario identification based on environmental conditions, facilitating the selection between Strategy 1 and Strategy 2 (see Figure 6). Additionally, this module allows for automatic adjustment of the exposure time for the BLAZE 101 sensors. The reason for having two strategies is that while the BLAZE 101 sensors perform well under various outdoor lighting conditions, a considerable percentage of point cloud information is lost in the presence of airborne particles, making them unusable. To address this, Strategy 2 employs images from the BLAZE 101 in combination with the RMS1000 and CERES V 640 sensors. However, this strategy is not part of the information presented in this research. Section 3 provides details regarding Strategy 1.

3. Results

This section presents the most relevant research results, analyzing single and close rocks to identify suitable impact points (Strategy 1). This development aligns with one of the core objectives of the project I+ D ID21I10087, which seeks to implement algorithms for rock dimensionalization. The following describes the results of the four stages considered for Strategy 1 (see Figure 6):

First stage: In the first registration stage, a predetermined transformation matrix is experimentally used to align both captures to a desired reference frame. This process enables the filtering of a region of interest containing the rocks, and additional filtering is applied along the z−axis to extract the plane containing the objects of interest. The segmented plane is assigned an identifier as an attribute (see Figure 8).

Second stage: The precomputed OCTREE structure organizes and efficiently connects the point cloud elements for the capture, which contain only the rocks. This study sets an OCTREE level of 6, defining a cell size slightly larger than 10 mm. This level establishes the minimum distance between two components; a higher level reduces this gap, allowing for the identification of a more significant number of connected components. Additionally, a threshold of 1000 minimum points per component is set to discard components with fewer points than this amount. This hierarchical subdivision enables the precise segmentation of each rock, which is assigned an identifier as an attribute (see Figure 9).

According to Poux [32], the connected−component labeling technique is one of the most critical processes for image analysis, computer vision, pattern recognition, and machine learning. Although primarily applied to 2D data, this technique can be extended to 3D structures using OCTREE.

Connected−component labeling is a key process for identifying and segmenting objects within an image or point cloud. A connected component (also called an object) is the largest set of pixels or points connected, enabling clustering to group points that belong to the same object or region. This process allows for recognizing and analyzing each object in the image or capture individually. For example, in a binary image of size $N \times N$, the pixel at coordinate (x, y) is denoted as $b(x, y)$, where $0 \leq x \leq N-1$ and $0 \leq y \leq N-1$. Foreground pixels (the objects) have a value of 1, while background pixels have a value of 0. Two pixels p and q are considered connected if there exists a path consisting of object pixels $a_1, a_2, \ldots, a_n$, where $a_1 = p$, and each a_i is a neighbor of a_{i+1} using the chosen connectivity. One available option is 4−connectivity, where the neighbors of a pixel $b(x, y)$ are the adjacent pixels in the horizontal and vertical directions: $b(x-1, y)$, $b(x+1, y)$, $b(x, y-1)$, $b(x, y+1)$ [38].

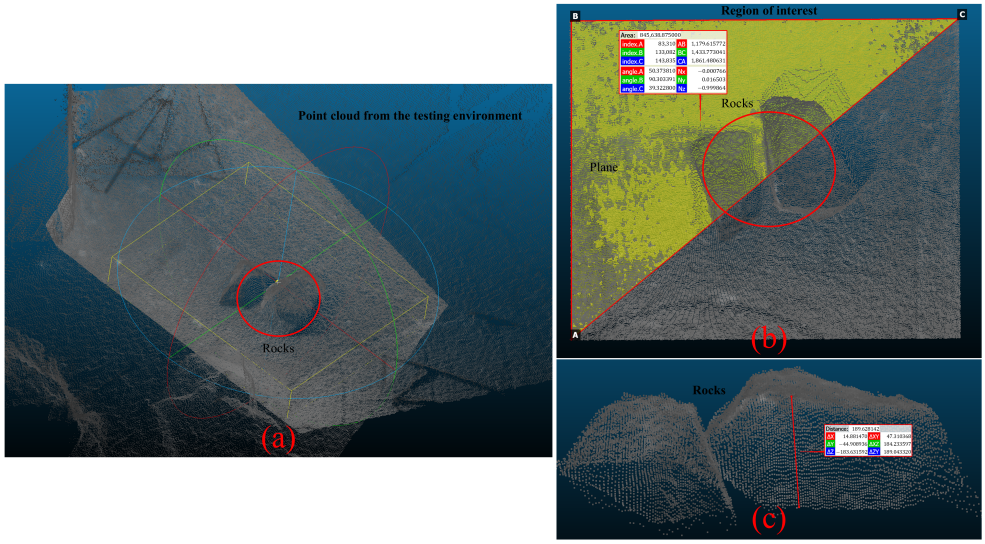

Figure 8. Point cloud filtering. (**a**) Merged point cloud. (**b**) Filtering of the region of interest. (**c**) Plane filtering.

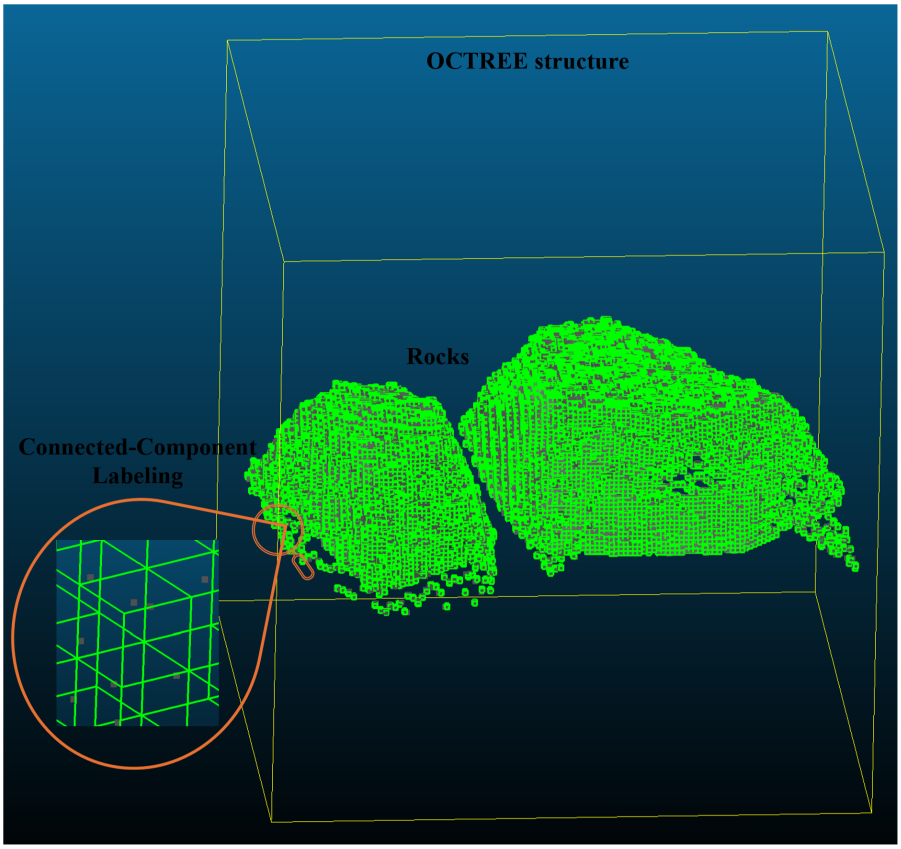

Figure 9. Component identification through OCTREE and connected−component labeling.

Third stage: Once labeling is complete, the characteristics of the identified objects are extracted and analyzed. Various properties are evaluated for each rock to determine which are the most effective for filtering potential impact points. Table 2 presents the analyzed characteristics [32,39,40].

Table 2. Equations and their descriptions.

Equation Number	Equation	Description
(4)	$\lambda_1, \lambda_2, \lambda_3$	Eigenvalue 1, eigenvalue 2, eigenvalue 3
(5)	$\sum_{i=1}^{3} \lambda_i$	Sum of eigenvalues
(6)	$PCA1$	-
(7)	$PCA2$	-
(8)	λ_v	Surface variation
(9)	λ_e	Eigentropy
(10)	λ_a	Anisotropy
(11)	λ_p	Planarity
(12)	λ_l	Linearity
(13)	λ_s	Sphericity
(14)	λ_o	Omnivariance
-	$\vec{v}_3$	Normal vector
(15)	λ_{ve}	Verticality

$$\lambda_1 \geq \lambda_2 \geq \lambda_3 \tag{4}$$

$$\sum_{i=1}^{3} \lambda_i = \lambda_1 + \lambda_2 + \lambda_3 \tag{5}$$

$$PCA1 = \frac{\lambda_1}{\sum_{i=1}^{3} \lambda_i} \tag{6}$$

$$PCA2 = \frac{\lambda_2}{\sum_{i=1}^{3} \lambda_i} \tag{7}$$

$$\lambda_v = \frac{\lambda_3}{\sum_{i=1}^{3} \lambda_i} \tag{8}$$

$$\lambda_e = -\sum_{i=1}^{3} \lambda_i \ln(\lambda_i) \tag{9}$$

$$\lambda_a = \frac{\lambda_1 - \lambda_3}{\lambda_1} \tag{10}$$

$$\lambda_p = \frac{\lambda_2 - \lambda_3}{\lambda_1} \tag{11}$$

$$\lambda_l = \frac{\lambda_1 - \lambda_2}{\lambda_1} \tag{12}$$

$$\lambda_s = \frac{\lambda_3}{\lambda_1} \tag{13}$$

$$\lambda_o = \sqrt[3]{\prod_{i=1}^{3} \lambda_i} \tag{14}$$

$$\lambda_{ve} = 1 - \left| z_{\vec{v}_3} \right| = \left| \left\langle \begin{bmatrix} 0 & 0 & 1 \end{bmatrix}, \vec{v}_3 \right\rangle \right| \tag{15}$$

The features are primarily derived from the data covariance matrix Σ of the points within each voxel as shown in Equation (16), where $\bar{X}$ is the mean vector as observed in Equation (17). From the obtained matrix, eigenvalues $(\lambda_1, \lambda_2, \lambda_3)$ and eigenvectors

($\vec{v}_1, \vec{v}_2, \vec{v}_3$) are calculated using Singular Value Decomposition (SVD). These eigenvectors represent the principal direction, its orthogonal direction, and the estimated normal [32,41]:

$$\Sigma = \frac{1}{m-1} \sum_{i=1}^{m} (X_i - \bar{X})(X_i - \bar{X})^T \tag{16}$$

$$\bar{X} = \frac{1}{m} \sum_{i=1}^{m} p_i \tag{17}$$

Different local neighborhood radii are used to calculate the characteristics: 5 mm, 10 mm, 15 mm, 20 mm, and 25 mm. Figure 10 shows the results for the 10 mm radius, while Figure 11 presents the histograms of these characteristics.

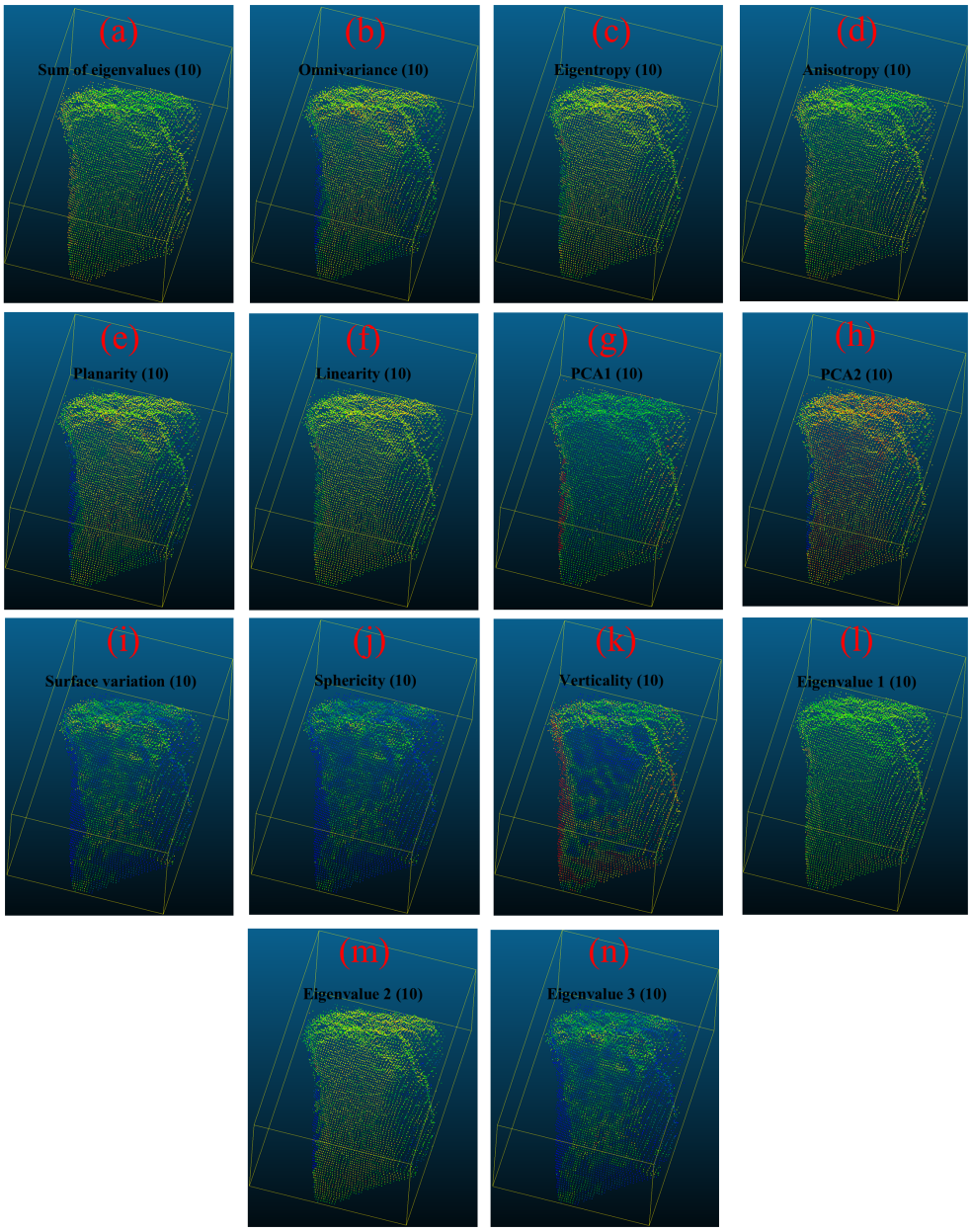

Figure 10. Characteristics computed with a 10 mm local neighborhood radius: (**a**) sum of eigenvalues, (**b**) omnivariance, (**c**) eigentropy, (**d**) anisotropy, (**e**) planarity, (**f**) linearity, (**g**) PCA1, (**h**) PCA2, (**i**) surface variation, (**j**) sphericity, (**k**) verticality, (**l**) eigenvalue 1, (**m**) eigenvalue 2, and (**n**) eigenvalue 3.

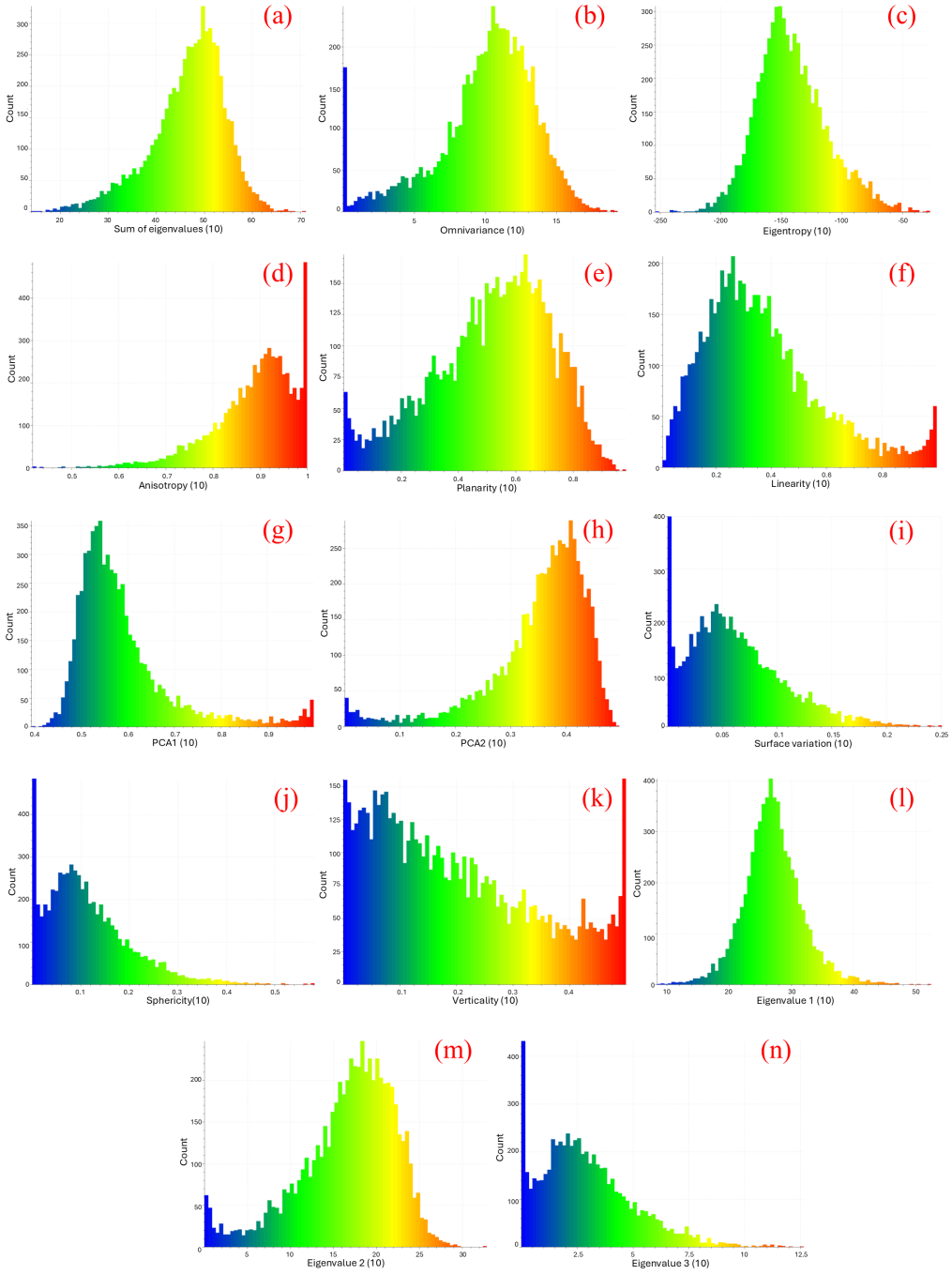

Figure 11. Histograms of characteristics computed with a 10 mm local neighborhood radius: (**a**) sum of eigenvalues, (**b**) omnivariance, (**c**) eigentropy, (**d**) anisotropy, (**e**) planarity, (**f**) linearity, (**g**) PCA1, (**h**) PCA2, (**i**) surface variation, (**j**) sphericity, (**k**) verticality, (**l**) eigenvalue 1, (**m**) eigenvalue 2, and (**n**) eigenvalue 3.

Figure 12 illustrates the verticality characteristic calculated with local neighborhood radii of 5 mm, 10 mm, 15 mm, 20 mm, and 25 mm.

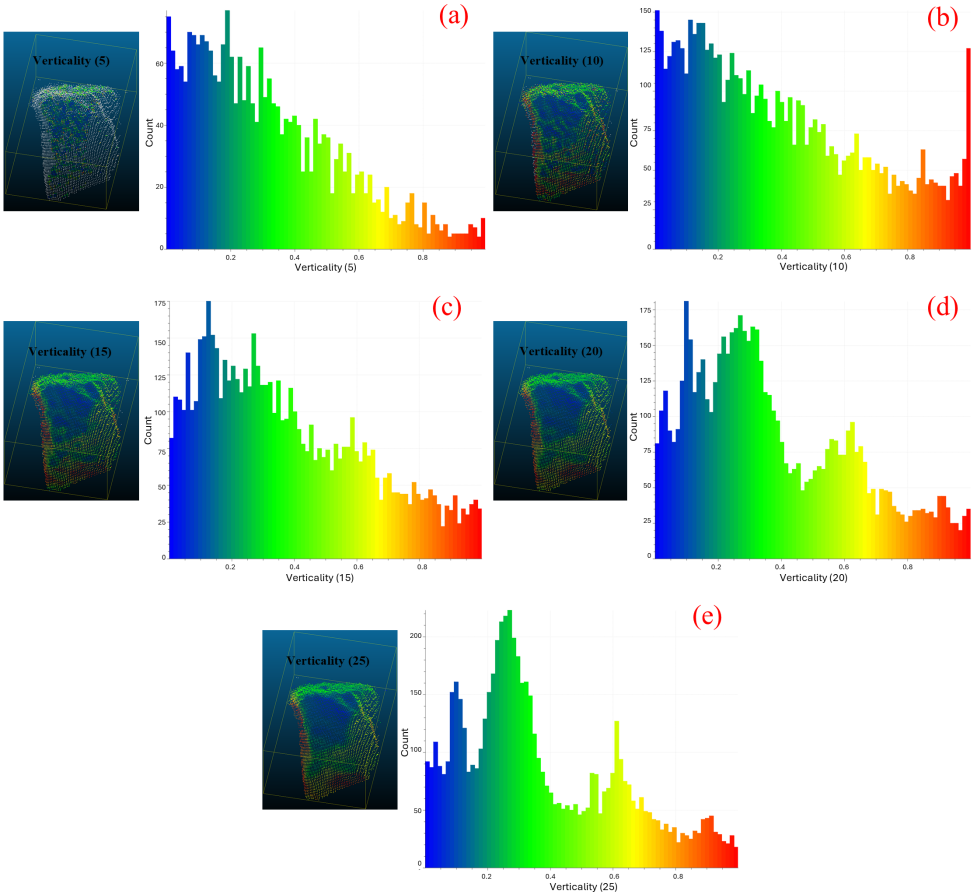

Figure 12. Histograms and verticality characteristic calculated with local neighborhood radii of (**a**) 5 mm, (**b**) 10 mm, (**c**) 15 mm, (**d**) 20 mm, and (**e**) 25 mm.

Figure 13 shows the different components of the normals computed with a 20 mm radius.

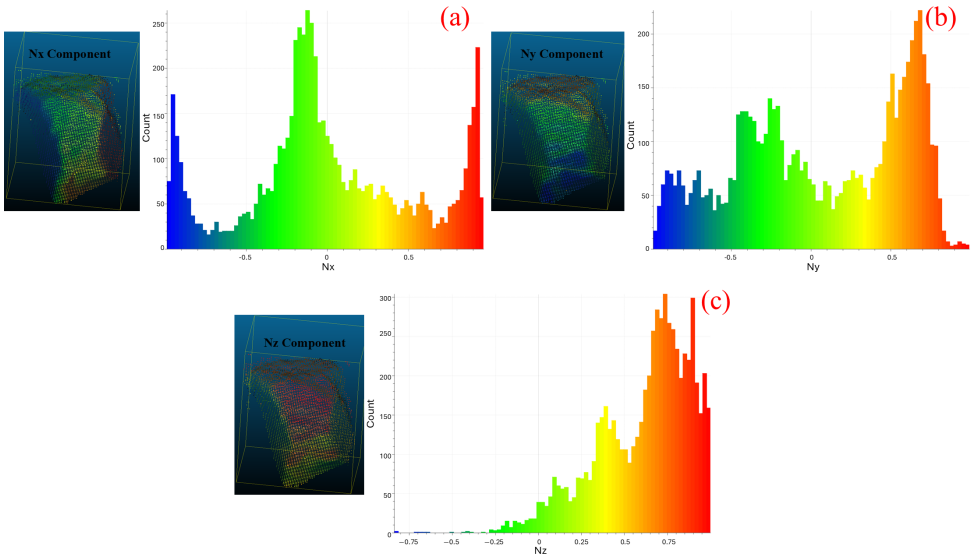

Figure 13. Histograms and normals calculated with a 20 mm radius: (**a**) Nx Component, (**b**) Ny Component, and (**c**) Nz Component.

Fourth stage: The faces of each rock are filtered based on the characteristic computed from the normals. The analysis of this characteristic identifies the face with the most significant area using two metrics: the number of points and the total surface area. Table 3 presents the values obtained for both metrics on each face of the rock. Additionally,

Figure 14 illustrates the filtered points according to the three components of the normals (Nx, Ny, and Nz).

Table 3. Characteristics of rock faces based on the normal component.

Face	Normal Component	Number of Points	Surface Area (mm^2)
Face 1	Nx	791	51,129.8
Face 2	Nx	976	67,949.3
Face 3	Ny	876	27,779.1
Face 4	Ny	2526	85,458.2
Face 5	Nz	1749	48,540.1

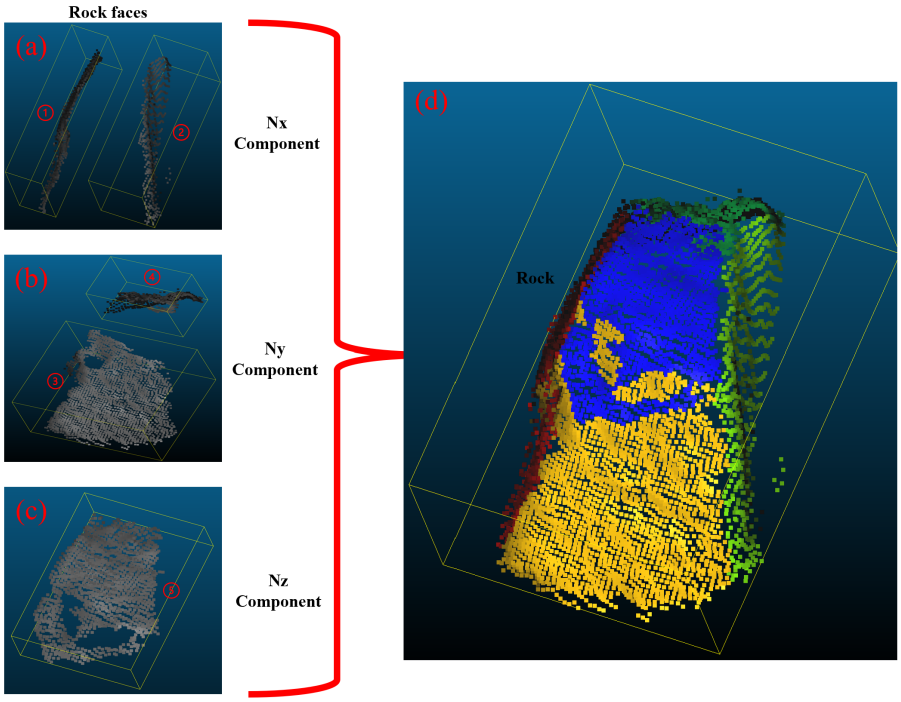

Figure 14. Filtered points based on normal components calculated with a 20 mm radius: (**a**) points filtered with the Nx component, (**b**) points filtered with the Ny component, (**c**) points filtered with the Nz component, and (**d**) object of interest.

This research uses the Ball−Pivoting Algorithm (BPA) technique for surface analysis and implements it with the open−source software MeshLab_64bit_fp v2023.12 [42].

The BPA is a widely used technique for reconstructing surfaces from an unorganized point cloud. This algorithm generates a triangular mesh that interpolates the provided points, typically samples of a surface obtained through multiple scans of an object (see Figure 15). This approach calculates the area of a surface reconstructed from a triangular mesh by summing the areas of all triangles in the mesh. The main steps of the algorithm are described below:

(a) Seed triangle selection: The algorithm selects an initial triangle that satisfies the condition that a sphere with radius p touches its three vertices without enclosing any other points within its interior.
(b) Sphere pivoting: While keeping the sphere in contact with two vertices of the current edge, the sphere pivots until it touches a new point. This new point and the two edge vertices form a new triangle.

(c) Mesh update: The new triangle is added to the mesh, and the algorithm moves on to consider the next edge for pivoting.

(d) Process repetition: The algorithm repeats the previous steps for all edges until it can no longer form additional triangles.

(e) Adapting to variable densities: If the sampling density is uneven, the algorithm can repeat the process using a sphere with a larger radius to cover areas with lower density [43].

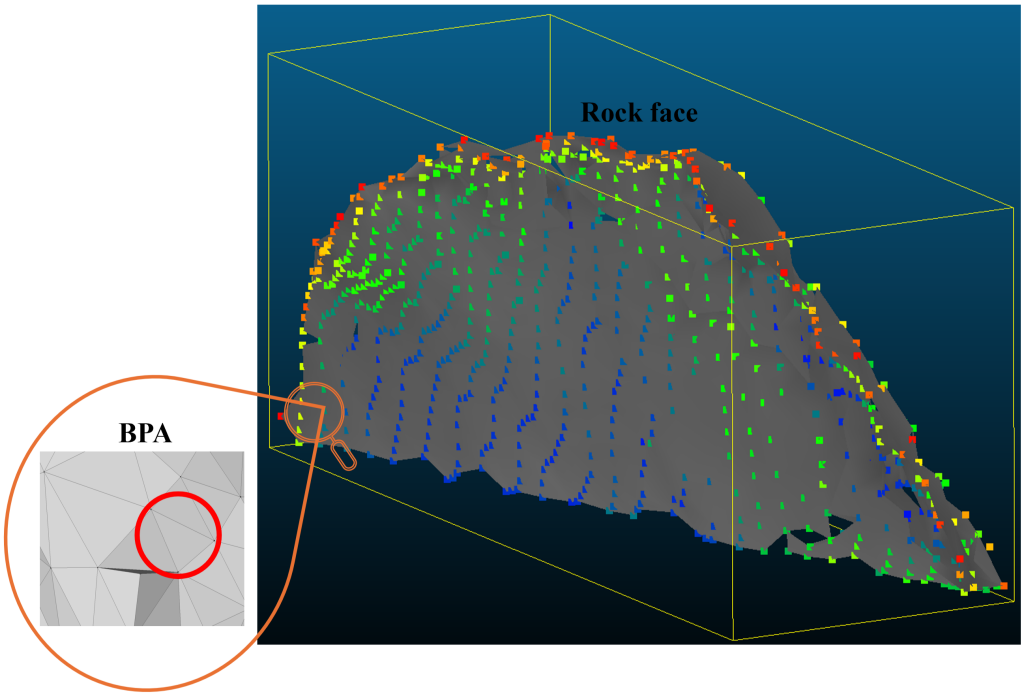

Figure 15. Surface reconstruction of a rock face using BPA.

Finally, this study presents an approach to reconstruct the rock face that aligns with the plane, where the point cloud provides no direct information (see Figure 16a).

(a) The proposed method reconstructs the plane's surface using the Poisson Surface Reconstruction technique implemented in the MeshLab_64bit_fp v2023.12 software (see Figure 16b). This technique generates closed meshes, effectively filling gaps in the point cloud that represents the plane. The process employs an OCTREE level of 6 while maintaining the other parameters at their default settings.

(b) The study converts the reconstructed surface into a new point cloud. It calculates the "Cloud−to−Cloud Distance" characteristic to compare this new cloud with the original point cloud representing the plane, using the CloudCompare 2.13.alpha software. The process employs an OCTREE level of 6 while maintaining the other parameters at their default settings (see Figure 16c). Notably, the calculation does not apply any local model; the distance between point clouds is determined simply by the nearest−neighbor distance, using an approach based on the Hausdorff distance algorithm.

(c) By analyzing the resulting histogram (see Figure 16d), the point cloud is filtered to identify and extract the missing face of the rock (see Figure 16e). The filtered face, labeled as face 6, contains 1968 points and has a surface area of 68,253.9 mm^2.

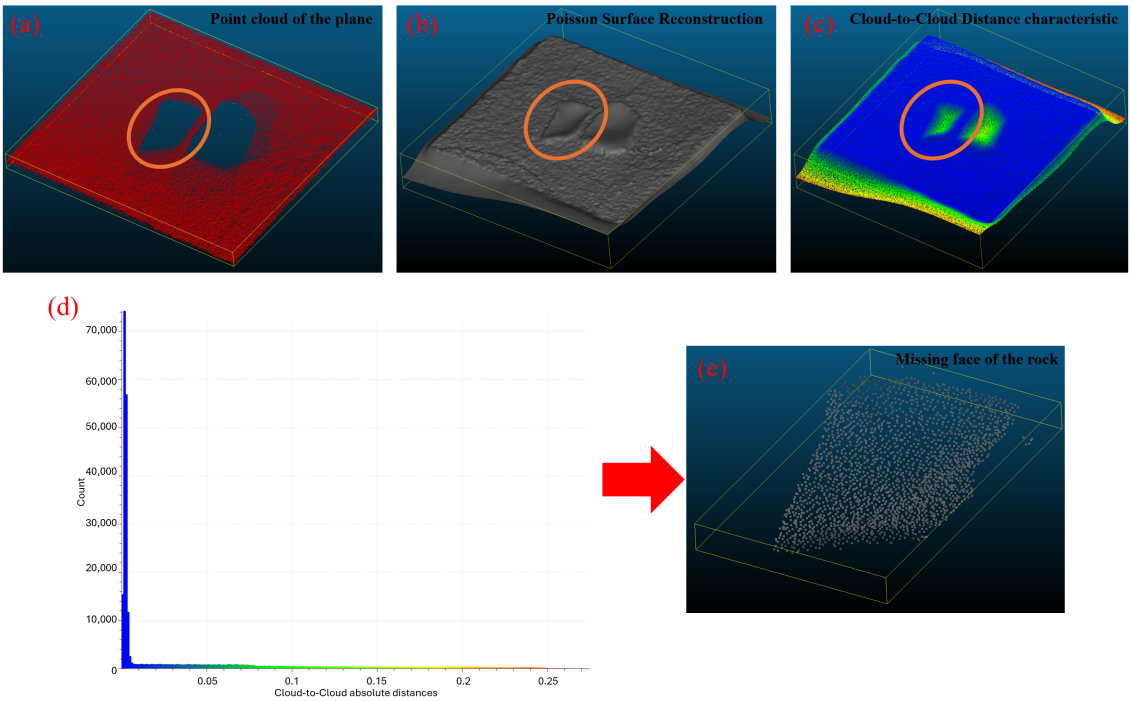

Figure 16. Extraction of the missing face in the analyzed rock using the Poisson Surface Reconstruction technique: (**a**) point cloud of the plane, (**b**) Poisson Surface Reconstruction technique applied to the plane, (**c**) computation of the Cloud-to-Cloud Distance characteristic, (**d**) histogram of the computation of the Cloud-to-Cloud Distance characteristic, and (**e**) filtered points of the point cloud.

The Poisson Surface Reconstruction technique reconstructs surfaces from unorganized oriented point sets. This technique is ideal for creating watertight meshes and is robust against noisy data. The method builds on the observation that the normal field of a solid's surface represents the gradient of an indicator function for the solid. The process for obtaining the reconstructed surface involves the following steps:

(a) Vector field construction: The process converts a set of oriented point samples into a continuous vector field within the three−dimensional space.

(b) Scalar function fitting: The process formulates a scalar function so that its derivative optimally aligns with the vector field generated from the point cloud normals. The process achieves this alignment by minimizing an energy function that measures the discrepancy between the gradient of the scalar function and the vector field, ensuring the reconstructed function closely follows the orientation of the computed normals:

$$E(\chi) = \int \|\nabla\chi(p) - \mathbf{V}(p)\|^2 \, dp, \tag{18}$$

where $\nabla\chi(p)$ represents the gradient of the function χ, and $\mathbf{V}(p)$ denotes the vector field.

(c) Poisson equation solution: The process solves the Poisson equation to obtain the scalar function that best fits the given vector field:

$$\Delta\chi = \nabla \cdot \mathbf{V}, \tag{19}$$

where Δ represents the Laplacian operator.

(d) System discretization: The system is discretized using an adaptive OCTREE structure, enabling the efficient management of the resolution and details of the reconstructed surface.

(e) Isosurface extraction: Finally, the isosurface corresponding to the zero level of the function χ is extracted, representing the reconstructed surface [44].

4. Discussion

This section analyzes the performance of the implemented data fusion system, considering both the quantitative and qualitative results obtained. It discusses the main strengths and limitations of the proposed approach, as well as the potential improvements and opportunities to enhance its application in future developments within the context of mining comminution.

- Data−level fusion enables the combination of information from sensors such as LiDAR and ToF cameras, contributing to more accurate and less noisy measurements, making it particularly useful for real−time applications. However, this approach also presents significant challenges, as it generates large volumes of data that can overwhelm the system memory and communication bandwidth. Additionally, achieving consistent alignment between measurements requires precise sensor calibration (registration), which can be challenging in incomplete measurements or data discrepancies. The resulting redundancy of information from this process further reduces fusion efficiency, impacting the overall system performance:
- The downsampling process significantly influences subsequent stages of data processing, particularly those reliant on distance calculations and normal analysis. While these techniques effectively reduce data density, maintaining a proper balance between the clarity of the object of interest and data representativeness proves crucial to minimizing errors in the later processing phases.
- The inherent complexity of analyzing scenarios with stacked rocks and the presence of elements like dust and fog introduce additional challenges in processing point clouds. Specific studies conducted within the framework of the project I + D ID21I10087, such as those by Rodríguez−Guillén et al. [23] and Kern et al. [20], have addressed these challenges in depth, providing a solid foundation for improving the accuracy of impact points under adverse environmental conditions.
- Using a calibration object during the point cloud registration process proves to be an effective technique for reducing processing times, enabling the precise alignment between captures from different sensors. This approach allows for more accurate filtering and delimitation of the region of interest, as the location of the object of interest (the impact zone where the rocks are situated in the experimental configurations) is known beforehand.
- Based on the results obtained from the computed characteristics and geometric analysis of the rocks, it is proposed that the most stable face for receiving impact is the one with the most extensive support surface. The 'x' and 'y' coordinates are determined using the centroid of this face's bounding box, while the 'z' coordinate is calculated as 50 % of the highest point detected on the rock. This approach aims to overcome the challenges associated with limited visibility during manual operations, reducing the application of unnecessary force and decreasing both downtime and energy consumption.
- According to the data obtained from the six faces of the analyzed rock, face 4 has the largest surface area (85,458.2 mm^2) and the highest number of points (2526). However, as shown in Table 3, there is not always a direct correlation between the number of points and the surface area of each face. This discrepancy could be related to the type of downsampling techniques implemented or the overlap of points in the point cloud, affecting surface representation accuracy.

- The Ball−Pivoting Algorithm (BPA) and the Screened Poisson Surface Reconstruction technique prove to be robust and efficient tools for reconstructing surfaces from point clouds. BPA excels in execution time and its ability to handle noisy data. Additionally, this algorithm enables the calculation of rock surface areas, regardless of point density or the presence of duplicates, as shown in Table 3. Conversely, the Screened Poisson Surface Reconstruction technique leverages the normals of the point cloud to solve the Poisson equation, generating a closed and smooth surface that significantly improves the reconstruction quality, even with irregular sampling. This technique is also essential for completing the missing information from the rocks not captured by the sensors, providing a more detailed and accurate surface reconstruction.
- The analysis of normals allows for the precise filtering of the rock faces represented in the point clouds, effectively identifying the surfaces relevant to the study. Additionally, in the surface reconstruction process using the Ball−Pivoting Algorithm (BPA) and the Screened Poisson Surface Reconstruction technique, the calculation of point cloud normals is essential. For BPA, the normals guide the sphere pivoting, ensuring the correct formation of the triangular mesh. In the case of the Screened Poisson technique, the normals play a critical role, as the process uses a normal vector field to solve the Poisson equation, generating a closed and smoothed surface from the point cloud data.
- The results obtained in this study form a fundamental part of the project I + D ID21I10087, which focuses on improving the comminution operations in the mining industry, specifically during the crushing process. This work provides a solid foundation for future research aimed at integrating additional modalities and developing advanced algorithms to identify the most effective impact points tailored to the specific characteristics of the rocks. Furthermore, subsequent research will include detailed analyses of processing times to address challenges associated with handling and transmitting large volumes of point cloud data. Finally, upcoming studies will investigate the potential energy savings and cost reductions achievable in the crushing stage when equipped with the proposed autonomy kit.

5. Conclusions

This study developed and implemented a multimodal data fusion system for the identification and impact of rocks in mining comminution tasks, demonstrating promising results in enhancing the efficiency of the crushing process. The analysis of the rocks' geometric characteristics identified the face with the most extensive support surface as the most suitable for receiving the impact, contributing to more excellent stability during fracture. This identification was facilitated by computing normals and precisely segmenting the relevant surfaces within the point cloud.

The implemented multisensory approach is pivotal in effectively addressing the challenges associated with adverse environmental conditions, such as dust and light variations, which impact visibility and accuracy in manual operations. The developed solution enables the precise identification of impact points. It creates new opportunities to reduce downtime and lower energy consumption during crushing tasks, achieved by reducing failed impacts and thereby improving operational efficiency.

This work lays a solid foundation for future research aimed at integrating new sensory modalities and developing more advanced algorithms to achieve the even more precise determination of impact points tailored to the specific characteristics of rocks and the operational conditions of the mining environment. These advancements are crucial for progressing toward an autonomous and robust system operating efficiently under extreme conditions.

Author Contributions: Conceptualization, D.F.Q.B. and J.K.; methodology, D.F.Q.B. and J.K.; software, D.F.Q.B. and J.K.; validation, D.F.Q.B. and J.K.; formal analysis, D.F.Q.B. and J.K.; investigation, D.F.Q.B. and J.K.; resources, D.F.Q.B. and J.K.; data curation, D.F.Q.B. and J.K.; writing—original draft preparation, D.F.Q.B. and J.K.; writing—review and editing, D.F.Q.B. and J.K.; visualization, D.F.Q.B. and J.K.; supervision, J.K. and C.U.; project administration, J.K. and C.U.; funding acquisition, J.K. and C.U. All authors have read and agreed to the published version of the manuscript.

Funding: This work has been supported by Agencia Nacional de Investigación y Desarrollo (ANID), Chile, through the IDeA I + D ID21I10087 project and the Vicerrectoría de Investigación, Innovación y Creación of the University of Santiago of Chile (USACH), Chile.

Data Availability Statement: The datasets presented in this article are not readily available because the data are part of an ongoing study.

Acknowledgments: We acknowledge and appreciate the support received from ANID Subdirección de Capital Humano/Doctorado Nacional/2022−21220739 for this research.

Conflicts of Interest: The authors declare no conflicts of interest.

References

1. Lynch, A. *Comminution Handbook*; The Australasian Institute of Mining and Metallurgy (AusIMM): Carlton, Australia, 2014.
2. Lampinen, S.; Niu, L.; Hulttinen, L.; Niemi, J.; Mattila, J. Autonomous robotic rock breaking using a real-time 3D visual perception system. *J. Field Robot.* **2021**, *38*, 980–1006. [CrossRef]
3. Correa, M.; Cárdenas, D.; Carvajal, D.; Ruiz-del Solar, J. Haptic Teleoperation of Impact Hammers in Underground Mining. *Appl. Sci.* **2022**, *12*, 1428. [CrossRef]
4. Cárdenas, D.; Parra-Tsunekawa, I.; Leiva, F.; Ruiz-del Solar, J. Automatic Determination of Rock-Breaking Target Poses for Impact Hammers. *Energies* **2022**, *15*, 6380. [CrossRef]
5. Samtani, P.; Leiva, F.; Ruiz-del Solar, J. Learning to Break Rocks With Deep Reinforcement Learning. *IEEE Robot. Autom. Lett.* **2023**, *8*, 1077–1084. [CrossRef]
6. Li, J.; Liu, Y.; Wang, S.; Wang, L.; Sun, Y.; Li, X. Visual perception system design for rock breaking robot based on multi-sensor fusion. *Multimed. Tools Appl.* **2024**, *83*, 24795–24814. [CrossRef]
7. Martirosyan, A.V.; Ilyushin, Y.V. The Development of the Toxic and Flammable Gases Concentration Monitoring System for Coalmines. *Energies* **2022**, *15*, 8917. [CrossRef]
8. Meng, T.; Jing, X.; Yan, Z.; Pedrycz, W. A survey on machine learning for data fusion. *Inf. Fusion* **2020**, *57*, 115–129. [CrossRef]
9. Ghamisi, P.; Rasti, B.; Yokoya, N.; Wang, Q.; Hofle, B.; Bruzzone, L.; Bovolo, F.; Chi, M.; Anders, K.; Gloaguen, R.; et al. Multisource and Multitemporal Data Fusion in Remote Sensing: A Comprehensive Review of the State of the Art. *IEEE Geosci. Remote Sens. Mag.* **2019**, *7*, 6–39. [CrossRef]
10. Yeong, D.J.; Velasco-Hernandez, G.; Barry, J.; Walsh, J. Sensor and Sensor Fusion Technology in Autonomous Vehicles: A Review. *Sensors* **2021**, *21*, 2140. [CrossRef] [PubMed]
11. Zhang, Y.; Sidibé, D.; Morel, O.; Mériaudeau, F. Deep multimodal fusion for semantic image segmentation: A survey. *Image Vis. Comput.* **2021**, *105*, 104042. [CrossRef]
12. Bokade, R.; Navato, A.; Ouyang, R.; Jin, X.; Chou, C.A.; Ostadabbas, S.; Mueller, A.V. A cross-disciplinary comparison of multimodal data fusion approaches and applications: Accelerating learning through trans-disciplinary information sharing. *Expert Syst. Appl.* **2021**, *165*, 113885. [CrossRef]
13. Quintero Bernal, D.F.; Kern, J.; Urrea, C. A Multimodal Fusion System for Object Identification in Point Clouds with Density and Coverage Differences. *Processes* **2024**, *12*, 248. [CrossRef]
14. Schreier, M. Data fusion for automated driving: An introduction. *Automatisierungstechnik* **2022**, *70*, 221–236. [CrossRef]
15. BASLER. Basler Product Documentation, Blaze-101. Available online: https://docs.baslerweb.com/blaze-101 (accessed on 15 May 2024).
16. SICK. Radar Sensors: RMS1000. Available online: https://www.sick.com/cl/es/catalog/productos/sensores-lidar-y-de-radar/sensores-de-radar/rms1000/rms1731c-636111/p/p660833?tab=detail (accessed on 15 May 2024).
17. Exosens. Ceres V 640 Series. Available online: https://www.exosens.com/products/ceres-v-640-series (accessed on 21 May 2024).
18. Nova Fitness Co., Ltd. Laser PM2.5 Sensor Specification, Product Model SDS011, Version V1.3. Available online: https://components101.com/sites/default/files/component_datasheet/SDS011-Sensor-Datasheet.pdf (accessed on 1 January 2025).
19. ROHM Co., Ltd. Digital 16bit Serial Output Type Ambient Light Sensor IC, BH1750FVI. Available online: https://dfimg.dfrobot.com/enshop/image/data/SEN0097/BH1750FVI.pdf (accessed on 1 January 2025).

20. Kern, J.; Rodriguez-Guillen, R.; Urrea, C.; Garcia-Garcia, Y. Enhancing 3D Rock Localization in Mining Environments Using Bird's-Eye View Images from the Time-of-Flight Blaze 101 Camera. *Technologies* **2024**, *12*, 162. [CrossRef]
21. Florea, H.; Petrovai, A.; Giosan, I.; Oniga, F.; Varga, R.; Nedevschi, S. Enhanced Perception for Autonomous Driving Using Semantic and Geometric Data Fusion. *Sensors* **2022**, *22*, 5061. [CrossRef]
22. Velasco-Hernandez, G.; Yeong, D.J.; Barry, J.; Walsh, J. Autonomous Driving Architectures, Perception and Data Fusion: A Review. In Proceedings of the 2020 IEEE 16th International Conference on Intelligent Computer Communication and Processing (ICCP), Cluj-Napoca, Romania, 3–5 September 2020; pp. 315–321. [CrossRef]
23. Rodriguez-Guillen, R.; Kern, J.; Urrea, C. Fast Rock Detection in Visually Contaminated Mining Environments Using Machine Learning and Deep Learning Techniques. *Appl. Sci.* **2024**, *14*, 731. [CrossRef]
24. Potter, H.; Kern, J.; Gonzalez, G.; Urrea, C. Energetically Optimal Trajectory for a Redundant Planar Robot by Means of a Nested Loop Algorithm. *Elektron. Elektrotechnika* **2022**, *28*, 4–17. [CrossRef]
25. Marrero, D.; Kern, J.; Urrea, C. A Novel Robotic Controller Using Neural Engineering Framework-Based Spiking Neural Networks. *Sensors* **2024**, *24*, 491. [CrossRef] [PubMed]
26. Kern, J.; Marrero, D.; Urrea, C. Fuzzy Control Strategies Development for a 3-DoF Robotic Manipulator in Trajectory Tracking. *Processes* **2023**, *11*, 3267. [CrossRef]
27. Lau, B.P.L.; Marakkalage, S.H.; Zhou, Y.; Hassan, N.U.; Yuen, C.; Zhang, M.; Tan, U.X. A survey of data fusion in smart city applications. *Inf. Fusion* **2019**, *52*, 357–374. [CrossRef]
28. Baroudi, U.; Al-Roubaiey, A.A.; Devendiran, A. Pipeline Leak Detection Systems and Data Fusion: A Survey. *IEEE Access* **2019**, *7*, 97426–97439. [CrossRef]
29. Wang, X.; Li, K.; Chehri, A. Multi-Sensor Fusion Technology for 3D Object Detection in Autonomous Driving: A Review. *IEEE Trans. Intell. Transp. Syst.* **2024**, *25*, 1148–1165. [CrossRef]
30. The MathWorks Inc. MATLAB Version 23.2.0.2515942 (R2023b) Update 7. Available online: https://www.mathworks.com (accessed on 1 January 2025).
31. CloudCompare. GPL Software (Version 2.13). Available online: http://www.cloudcompare.org (accessed on 2 May 2024).
32. Poux, F. The Smart Point Cloud: Structuring 3D Intelligent Point Data. Ph.D. Thesis, Université de Liège, Liège, Belgium, 2019.
33. Alberto, L.N.E. Algoritmos para el Pre Procesamiento de Nubes de Puntos Mediante Representaciones Dispersas. Ph.D. Thesis, Universidad Nacional, Bogota, Colombia, 2020.
34. Chen, S.; Liu, B.; Feng, C.; Vallespi-Gonzalez, C.; Wellington, C. 3D Point Cloud Processing and Learning for Autonomous Driving. *arXiv* **2020**. [CrossRef]
35. Que, Z.; Lu, G.; Xu, D. VoxelContext-Net: An Octree based Framework for Point Cloud Compression. *arXiv* **2021**. [CrossRef]
36. Cheng, L.; Chen, S.; Liu, X.; Xu, H.; Wu, Y.; Li, M.; Chen, Y. Registration of Laser Scanning Point Clouds: A Review. *Sensors* **2018**, *18*, 1641. [CrossRef] [PubMed]
37. Open3D. ICP Registration — Open3D 0.12.0 Documentation. Available online: https://www.open3d.org/docs/0.12.0/tutorial/pipelines/icp_registration.html (accessed on 8 July 2024).
38. He, L.; Ren, X.; Gao, Q.; Zhao, X.; Yao, B.; Chao, Y. The connected-component labeling problem: A review of state-of-the-art algorithms. *Pattern Recognit.* **2017**, *70*, 25–43. [CrossRef]
39. Demantké, J.; Vallet, B.; Paparoditis, N. Streamed Vertical Rectangle Detection in Terrestrial Laser Scans for Facade Database Production. *ISPRS Ann. Photogramm. Remote Sens. Spat. Inf. Sci.* **2012**, *3*, 99–104. [CrossRef]
40. Hackel, T.; Wegner, J.D.; Schindler, K. Contour Detection in Unstructured 3D Point Clouds. In Proceedings of the 2016 IEEE Conference on Computer Vision and Pattern Recognition (CVPR), Las Vegas, NV, USA, 27–30 June 2016; pp. 1610–1618. [CrossRef]
41. Blomley, R.; Weinmann, M.; Leitloff, J.; Jutzi, B. Shape distribution features for point cloud analysis—A geometric histogram approach on multiple scales. *ISPRS Ann. Photogramm. Remote Sens. Spat. Inf. Sci.* **2014**, *2*, 9–16. [CrossRef]
42. Cignoni, P.; Callieri, M.; Corsini, M.; Dellepiane, M.; Ganovelli, F.; Ranzuglia, G. MeshLab: An Open-Source Mesh Processing Tool. In Proceedings of the Eurographics Italian Chapter Conference, Salerno, Italy, 2–4 July 2008; Scarano, V., Chiara, R.D., Erra, U., Eds.; The Eurographics Association: Eindhoven, The Netherlands, 2008. [CrossRef]
43. Bernardini, F.; Mittleman, J.; Rushmeier, H.; Silva, C.; Taubin, G. The ball-pivoting algorithm for surface reconstruction. *IEEE Trans. Vis. Comput. Graph.* **1999**, *5*, 349–359. [CrossRef]
44. Kazhdan, M.; Hoppe, H. Screened poisson surface reconstruction. *ACM Trans. Graph.* **2013**, *32*, 1–3. [CrossRef]

Disclaimer/Publisher's Note: The statements, opinions and data contained in all publications are solely those of the individual author(s) and contributor(s) and not of MDPI and/or the editor(s). MDPI and/or the editor(s) disclaim responsibility for any injury to people or property resulting from any ideas, methods, instructions or products referred to in the content.